Supplementary Information for

Graphene-like monolayer monoxides and monochlorides: a two-dimensional family

Bingcheng Luo[1, 2, 3*], Yuan Yao[1], Enke Tian[1*], Hongzhou Song[4], Xiaohui Wang[2], Guowu Li[5], Kai Xi[6], Baiwen Li[4], Haifeng Song[4], Longtu Li[2]

[1] School of Science, China University of Geosciences, Beijing 100083, P. R. China
[2] State Key Laboratory of New Ceramics and Fine Processing, School of Materials Science and Engineering, Tsinghua University, Beijing 100084, P. R. China
[3] Department of Engineering, University of Cambridge, Cambridge CB3 0FA, United Kingdom
[4] Institute of Applied Physics and Computational Mathematics, Beijing 100094, P. R. China
[5] Crystal Structure Laboratory, National Laboratory of Mineral Materials, China University of Geosciences, Beijing 100083, P. R. China
[6] Department of Materials Science and Metallurgy, University of Cambridge, Cambridge CB3 0FS, United Kingdom

This PDF file includes:

Supplementary text
Figs. S1 to S18
Tables S1 to S6
References for SI reference citations

Supplementary Information Text

Methods

Candidate structures were searched using a particle-swarm optimisation (PSO) method within an evolutionary algorithm, as implemented in CALYPSO code (1, 2). This has been successfully applied to predict stable 2D boron-carbon compounds (3), 2D FeB$_6$ monolayers (4), 2D Cu$_2$Si monolayers (5), 2D boron hydride sheets (6), 2D ionic boron (7), and 2D electrides (8). In our PSO calculations, the population size was set to 1000, and the number of generations was maintained at 50. The required structural relaxations were performed using a PBE functional implemented in VASP code. After obtaining the most stable 2D monolayers, we placed each in the *xy*-plane with the z-direction perpendicular to the layer plane. A vacuum space of 15 Å in the z-direction was adopted to avoid interactions between adjacent layers.

First-principle calculations were performed by employing a pseudopotential plane-wave (PP-PW) approach based on density functional theory (DFT) framework, as implemented in the Cambridge Serial Total Energy (CASTEP) code. CASTEP is a density functional theory-based pseudopotential total-energy code that employs special point integration over the Brillouin zone and has a plane-wave basis set for the expansion of wave functions (9). Norm-conserving pseudopotentials in the Kleinman–Bylander form (10) were used to describe the electron-ion interactions. The generalised gradient approximated (GGA) functional of Perdew−Burke−Ernzerhof for solid (PBEsol) exchange-correlation functional was used (11). The Broyden–Fletcher–Goldfarb–Shannon (BFGS) minimiser was employed to carry out unit cell optimisation (12). For the plane wave basis, we selected a high cut-off energy of 830 eV. The Brillouin zone was sampled with an $11 \times 11 \times 1$ Γ-centered Monkhorst−Pack k-points grid for geometry optimisation and self-consistent calculations. The energy tolerance was 5×10^{-6} eV per atom, the force tolerance was 0.001 eV Å^{-1}, the stress tolerance was 0.02 GPa, and the displacement tolerance was 5×10^{-4} Å.

To strengthen the validation of these calculations, we also used projector-augmented wave (PAW) pseudopotentials in a Vienna *ab initio* simulation program (VASP) for structural relaxation and determination of properties (13, 14). A kinetic energy cutoff of plane-wave basis expansion was set to 600 eV. The First Brillouin zone was sampled using an automatically generated $11 \times 11 \times 1$ Monkhorst−Pack set of k points (15). In all these calculations the convergence criteria for total energy in the self-consistent field iteration was set to 1×10^{-8} eV, and geometry optimisations were carried out by full relaxations until the Hellmann−Feynman force component on each atom was less than 0.001 eV/Å. SCAN meta-GGA functional, and Heyd−Scuseria−Ernzerhof (HSE) screened hybrid functional (16, 17) are adopted to obtain the accurate band structure.

To evaluate the kinetic stability of these new graphene-like monolayer monoxides and monochlorides, phonon dispersion analysis was employed. This used density functional perturbation theory (DFPT) with a linear response method implemented in CASTEP code (18). To evaluate the thermal stability of new graphene-like monolayers, *ab initio* molecular dynamics (AIMD) simulations were performed using the PAW method and a GGA-PBEsol functional in CASTEP and VASP code. During MD simulations, initial configurations of the 2D monolayers in 3×3 supercells were annealed at different temperatures, with each MD simulation in the NVT ensemble lasting for 10 ps with a time

step of 2.0 fs. The temperature was controlled using Nosé−Hoover thermostats (19, 20) in the temperature range from 300 K to 3500 K.

Bader charge analysis was performed using code developed by Henkelman's group (21–23). Bader analysis uses zero flux surfaces to divide atoms, and the analysis is merely dependent on charge density distribution. The charge enclosed within the Bader volume is a good approximation to the total electronic charge of an atom. Mulliken atomic population analysis (24, 25) and Hirschfeld analysis (26, 27) were also performed for comparison.

2D graphene-like structure without d-orbital.

Several rock-salt-like binary compounds were filtered out and screened from the structure database. We then focused on some additional common materials with fewer or no d-orbitals, such as CaO, SrO, BaO, and HfO as shown in Figure S1. By using a particle swarm structural search (1) and first-principle calculations based on both density functional theory (DFT) and density functional perturbation theory (DFPT) (18, 28).

2D graphene-like structure containing d-orbital

Moreover, we also studied the rock-salt-like binary compounds containing d-orbitals, such as AgCl, HfO, and CdO for comparison and further verification. All these materials maintain a graphene-like structure within a one-atom-thickness planar hex-coordinate lattice.

Fig. S1 and Fig. S2 show the 2D structure of CaO, SrO, BaO, and HfO monolayer sheets. Table S1 and Table S2 show the lattice parameters of bulk rock-salt-like binary compounds and their corresponding two-dimensional structure.

Scanning tunneling microscopy analysis

Scanning tunneling microscopy (STM) analysis of the discovered 2D monolayers were simulated based on the Tersoff and Hamann approximation (29) at constant height mode used to mimic the experimental setup (30). Fig. S3A shows the simulated STM images of graphene for comparison, which is in great agreement with the experimental results (31, 32). For single-layer sheets of graphene, the asymmetry of graphite bulk is removed (32). All surface carbon atoms of graphene are identical, and a symmetrical honeycomb structure can be clearly observed in the simulated STM image. Fig. S3 B-F show the simulated STM images of discovered 2D BaO, AgCl, HfO, BeO, and CdO monolayers, respectively. The simulated STM images of 2D BaO sheets, 2D AgCl sheets, and 2D CdO sheets show surfaces with a hexagonal pattern, while the simulated STM images of 2D BeO sheets and 2D HfO sheets reveal surfaces with triangular patterns. These outcomes will be useful in identifying and distinguishing future experimental STM images.

Binding energy using different pseudopotentials

The binding energy (E_b) of these 2D materials is calculated with the formula $E_b = E_{AB} - E_A - E_B$, where E_{AB}, E_A, and E_B are the energy of 2D monolayer compound AB, their constituent atoms A and B, respectively. The Fig. S4 shows the binding energy calculated using different pseudopotential schemes: the projector augmented wave (PAW) method

and norm-conserving pseudopotentials (NCP). The binding energy of graphene calculated using different pseudopotential shows the same value. For the predicted 2D materials, binding energy using norm-conserving pseudopotential is a bit higher than the binding energy using PAW pseudopotential. All the binding energy are negative by using different pseudopotential, indicating the stability of 2D monolayers.

Analysis of kinetic stability

The kinetic stability of the presented two-dimensional materials is performed by calculating the phonon dispersion using DFPT methods along the high-symmetry lines in the Brillouin zone.

Fig. S5 shows the calculated phonon dispersion of pristine graphene for comparison, which is in great agreement with the experimental and other theoretical results (33–35).

Similar to graphene (36–38), these 2D monolayers have six phonon branches: out-of-plane acoustic (ZA) and out-of-plane optical (ZO) phonons, where Z indicates that the displacement vector is along the Z axis; transverse acoustic (TA), transverse optical (TO), longitudinal acoustic (LA) and longitudinal optical (LO) phonons, which correspond to vibrations within the 2D plane. All frequencies were positive, with no appearance of imaginary phonon modes, indicating that the graphene-like monoxides and monochlorides are thermodynamic stable.

Discovery of graphene-like mononitride monolayer

Adopting the same strategy in present work, we further studied the other rock-structure binary mononitrides such as scandium nitride (ScN) as seen in Fig. S6.

Fig. S7 shows the phonon dispersion curve of predicted 2D ScN monolayer. All frequencies were positive, with no appearance of imaginary phonon modes, indicating that the graphene-like ScN is thermodynamic stable.

Discovery of graphene-like monoselenide monolayer

Adopting the same strategy in present work, we further studied the other rock-structure binary monoselenides such as cadmium selenide (CdSe). Fig. S8 shows the 2D structure of CdSe monolyer.

Fig. S10 shows the phonon dispersion curve of predicted 2D ScN monolayer. Unfortunately, the frequencies at Gamma point are positive, while the frequencies at K and M points were negative. This reveals the metastable character of 2D CdSe monolayer.

Stress engineering on the stability of graphene-like monoselenide monolayer

To address the above issue of metastability of predicted 2D CdSe monolayer, we tried to apply the external stress on the 2D CdSe monolayer structure.

The results show that the negative frequency can be converted to positive by considering the effects of external stress, as shown in Fig. S9 and Fig. S10. This indicates that ambient stresses can help stabilise 2D CdSe monolayers.

Accurate band structure analysis

Note that GGA calculations tend to underestimate the bandgaps of semiconducting materials. To obtain the more accurate band structure, we adopted SCAN meta-GGA functional, and Heyd−Scuseria−Ernzerhof screened hybrid functionals (HSE) (16, 17). The

semi-local meta-GGA strives to be more accurate than GGA for a broader range of applications and chemical systems (39–41). Recently developed non-empirical strongly constrained and appropriately normed (SCAN) meta-generalized gradient approximation functional has been reported to predict accurate geometries and energies of diversely bonded molecules and materials, including covalent, metallic, ionic, hydrogen and van der Waals bonds (39, 42). The more accurate HSE06 exchange functional was also used. HSE functional incorporating a fraction of Hartree−Fock (HF) exchange into short-range exchange interactions has been proposed and successfully applied to strong correlation systems (43). The resulting expression for the exchange-correlation energy is given by:

$$E_{xc}^{HSE} = aE_x^{HF,SR}(\mu) + (1-a)E_x^{PBE,SR}(\mu) + E_x^{PBE,LR}(\mu) + E_c^{PBE} \tag{1}$$

As can be seen above, the exchange energy (E_{xc}^{HSE}) is separated into a short-range and long-range component, labelled SR an LR, respectively. The SR part includes both HF ($E_x^{HF,SR}$) and PBE ($E_x^{PBE,SR}$) terms, while the LR part has only one PBE ($E_x^{PBE,LR}$) term. Here, a is the HF exchange mixing coefficient, and μ is a splitting parameter that defines the partitioning between the SR and LR components, which was adjusted to reproduce PBE hybrid heats of formation in molecules with some consideration given to band gaps in materials (16, 17). For the standard HSE06 functional, the parameter a was chosen as 0.25, which can accurately predict enthalpies of formation, ionisation potentials, and electron affinities for molecules as well as lattice constants and band gaps for solids (16).

Fig. S14 shows the band structure of other 2D materials mentioned in the manuscripts. As seen, the calculated band gaps using GGA-PBEsol are in good accordance with the band gaps using SCAN. Within the SCAN meta-GGA exchange functional, the band structure is slightly improved, yet greater improvement is achieved using the HSE06 hybrid functional as seen in Fig. S14.

Analysis of Mechanic stability

The elastic constants are critical parameters for mechanical properties of materials. The elasticity tensor, *Cij*, of both 2D MgO monolayer and 2D NaCl monolayer were computed from the first derivatives of the stresses computed in VASP. Table S4 and Table S5 show the Cij matrix of 2D MgO monolayer and 2D NaCl monolayer. It is found that the elastic matrix for both monolayers are symmetric, i.e., $C_{ij}=C_{ji}$. Table S4 and Table S5 show the calculated eigenvalues of the elastic matrix. The matrix C and all eigenvalues of C are positive, indicating the elastic stability. The Born stability criteria for the stability of hexagonal system are

(i) $C_{11}-C_{12}>0$;

(ii) $2 \times C_{13} \times C_{13} < C_{33} \times (C_{11}+C_{12})$;

(iii) $C_{44}>0$.

From Table S4, we can see that all three conditions for both 2D NaCl monolayer and 2D MgO monolayer are satisfied, revealing the stability.

Electron charge analysis

Bader charge analysis was performed using code developed by Henkelman's group (21–23). Bader analysis uses zero flux surfaces to divide atoms, and the analysis is merely dependent on charge density distribution. The charge enclosed within the Bader volume is a good approximation to the total electronic charge of an atom. Mulliken atomic population analysis (24, 25) and Hirschfeld analysis (26, 27) were also performed for comparison.
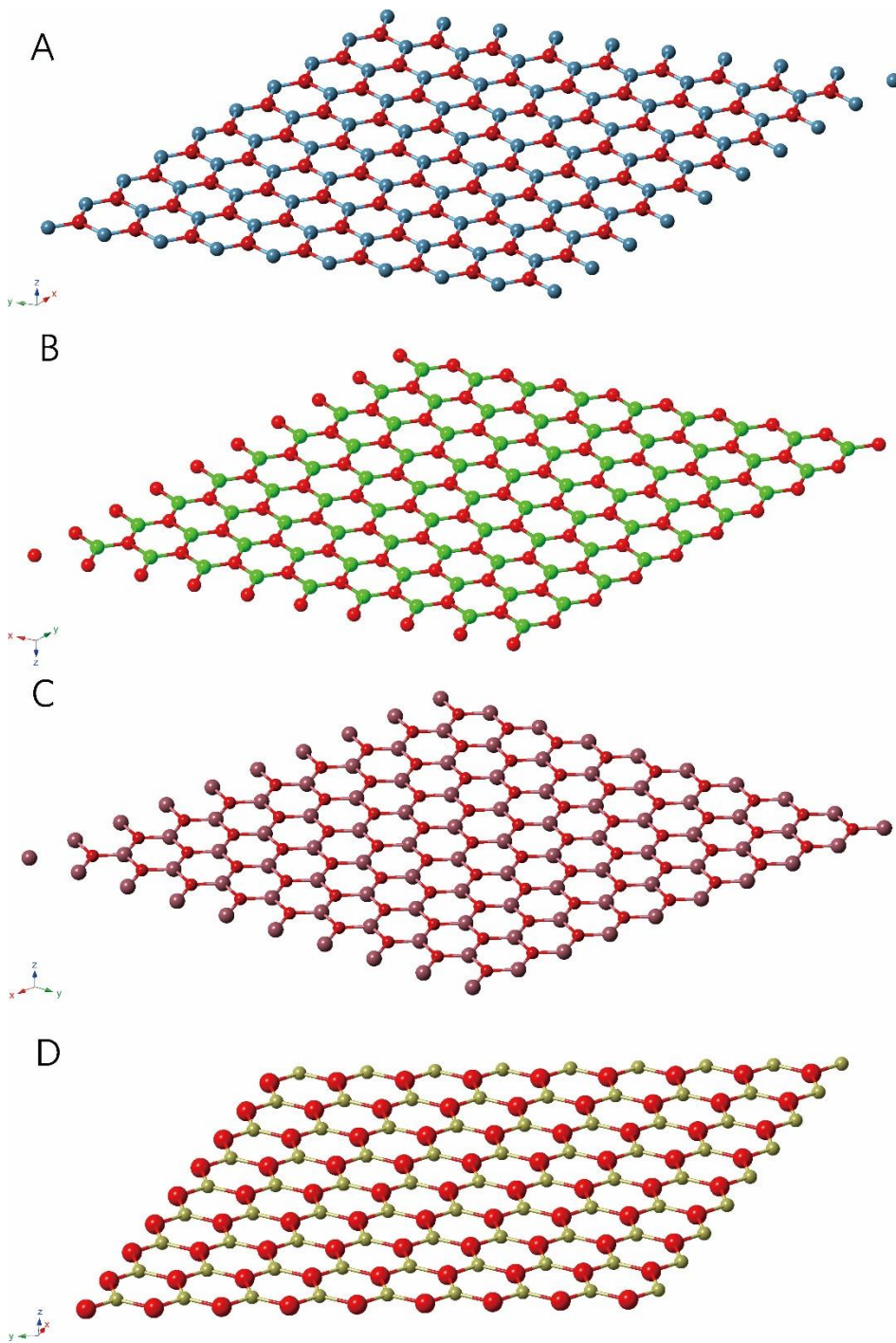
Supplementary Figures

Fig. S1 3D view of two-dimensional (A) CaO, (B) SrO, (C) BaO, and (D) HfO monolayer sheets.
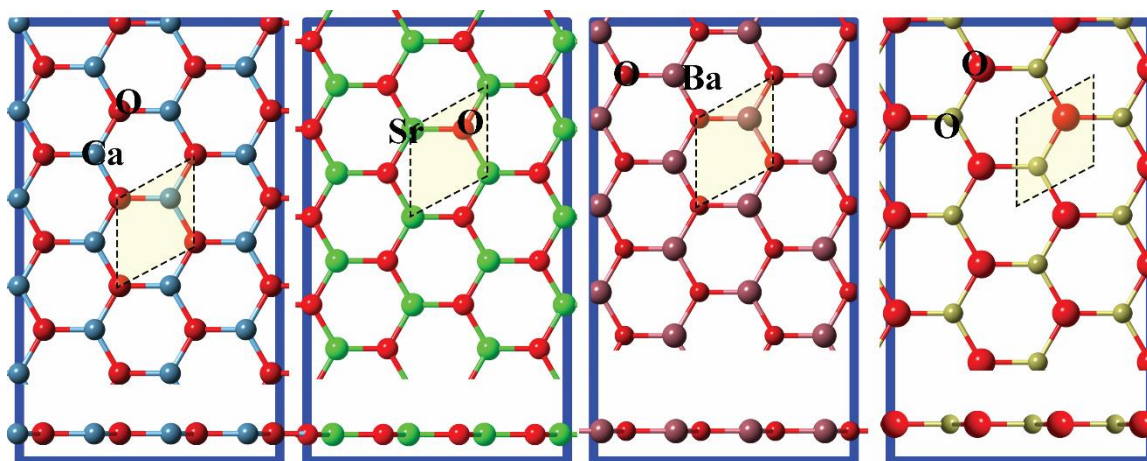
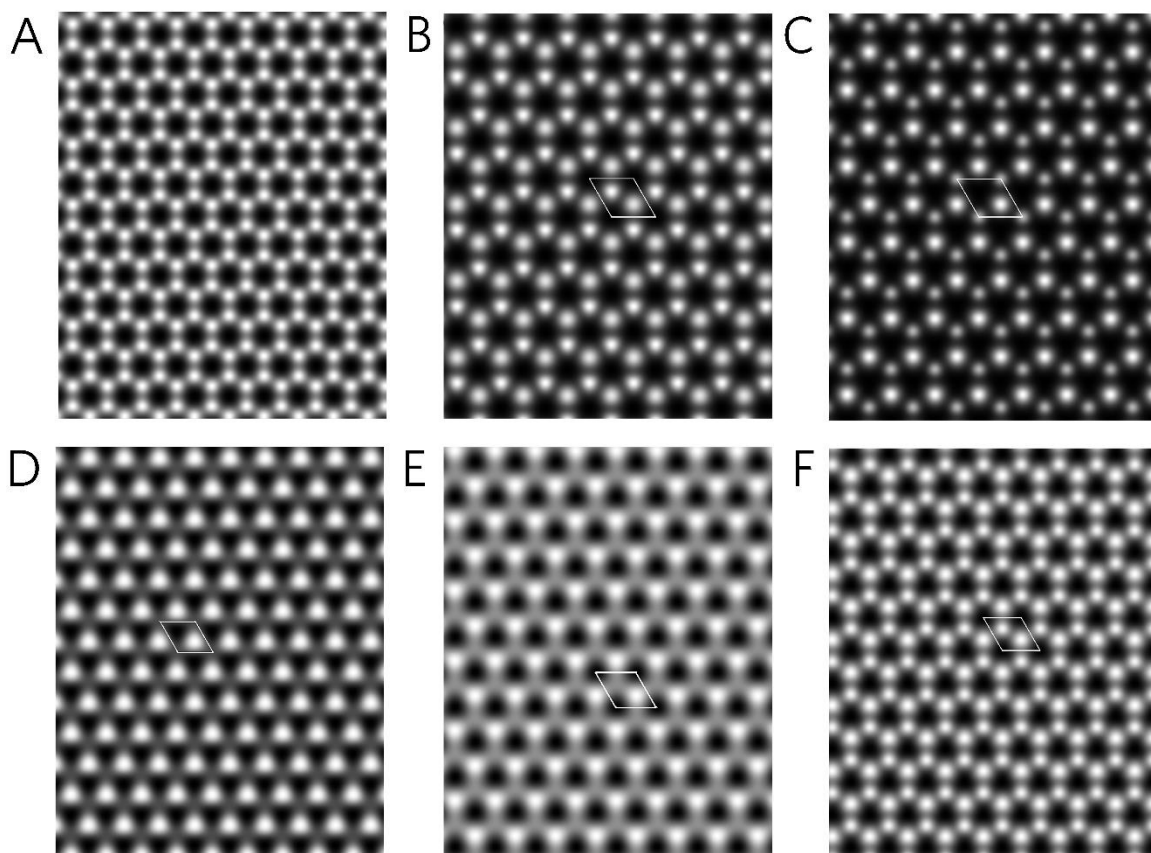Fig. S2 Planar and side view of 2D CaO, SrO, BaO, and HfO monolayer sheets.

Fig. S3 The simulated STM images of graphene (A) and predicted 2D monolayers: (B) BaO, (C) AgCl, (D) HfO, (E) BeO, and (F) CdO.
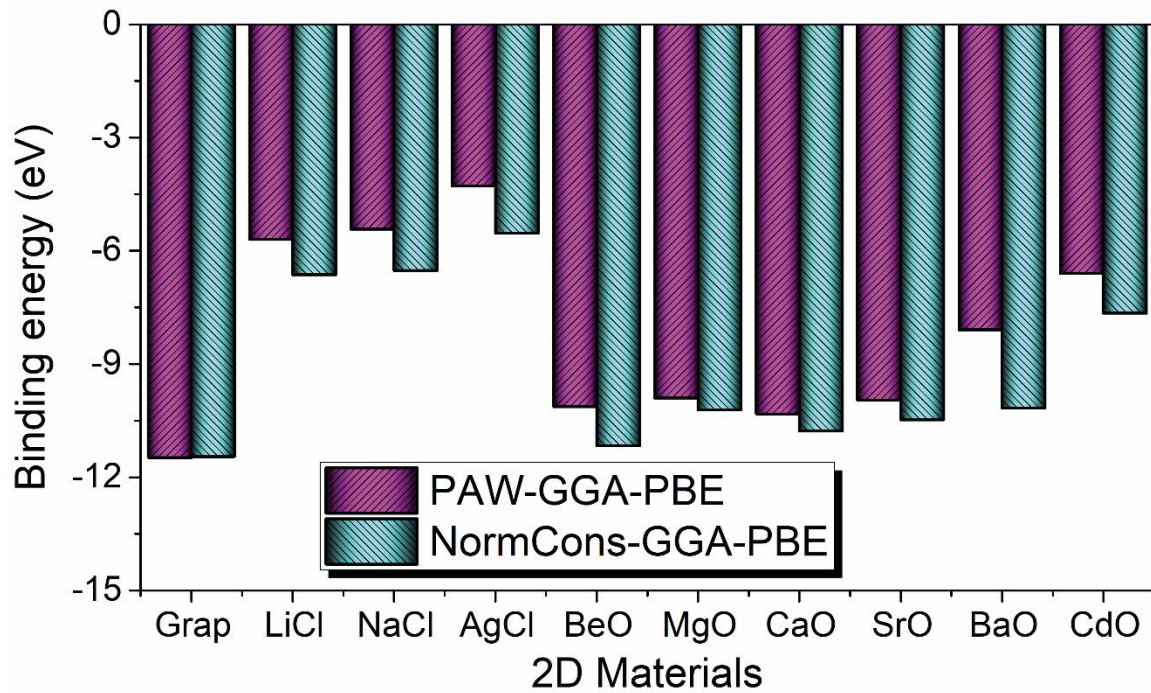
Fig. S4 Binding energy of 2D materials calculated using PAW and norm conserving
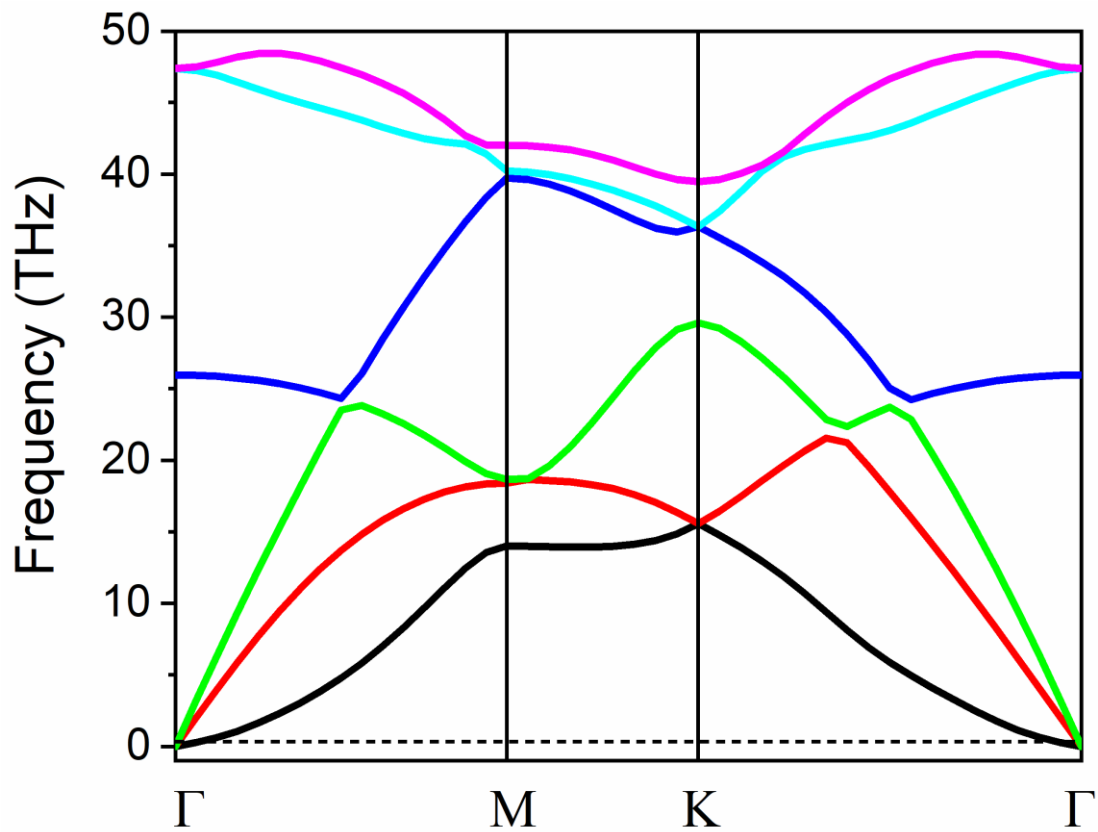
pseudopotential

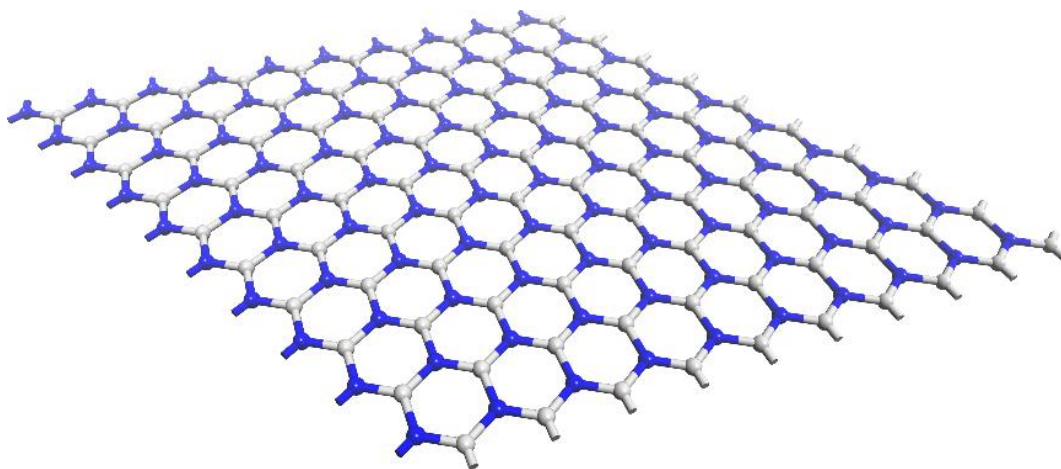Fig. S5 Phonon dispersion of graphene.

Fig. S6 Two-dimensional structure of ScN monolayer. White sphere is Sc atom and blue
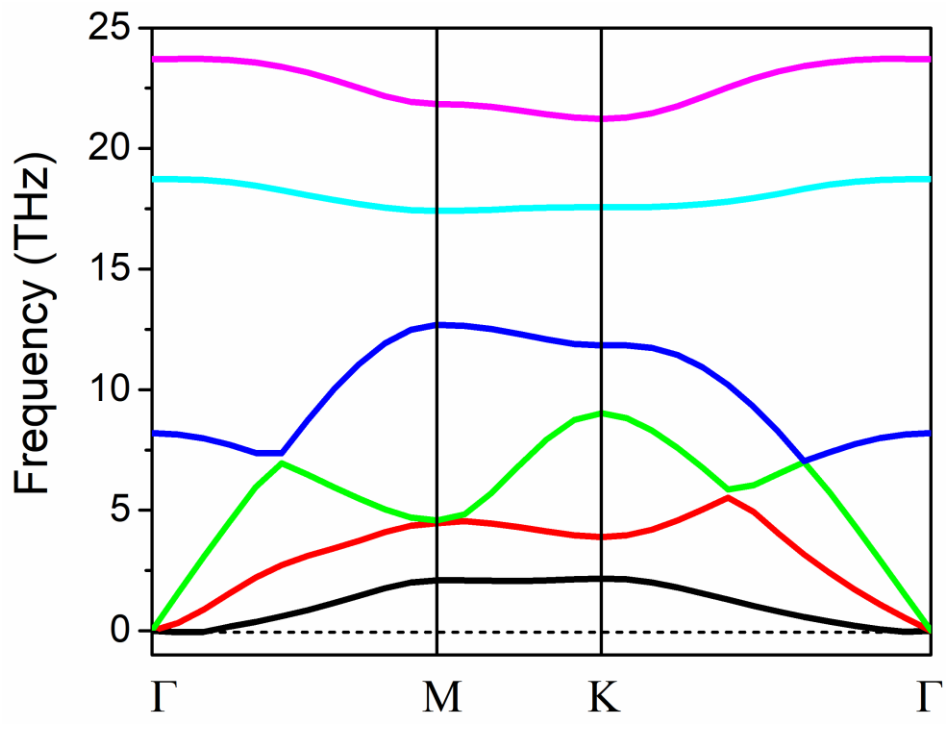
sphere is N atom.

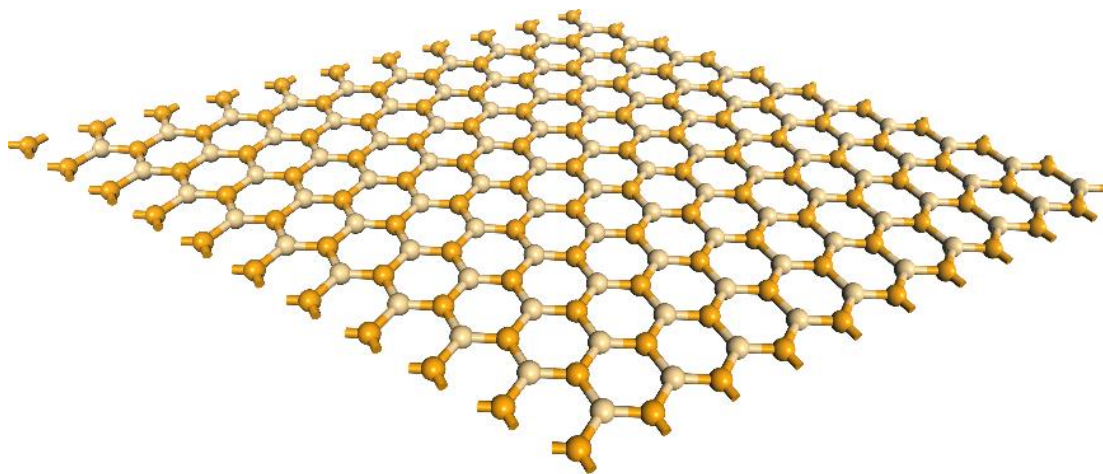Fig. S7 Phonon dispersion of 2D ScN monolayer.

Fig. S8 Two-dimensional structure of CdSe monolayer. Orange sphere is Cd atom and light-yellow sphere is Se atom.
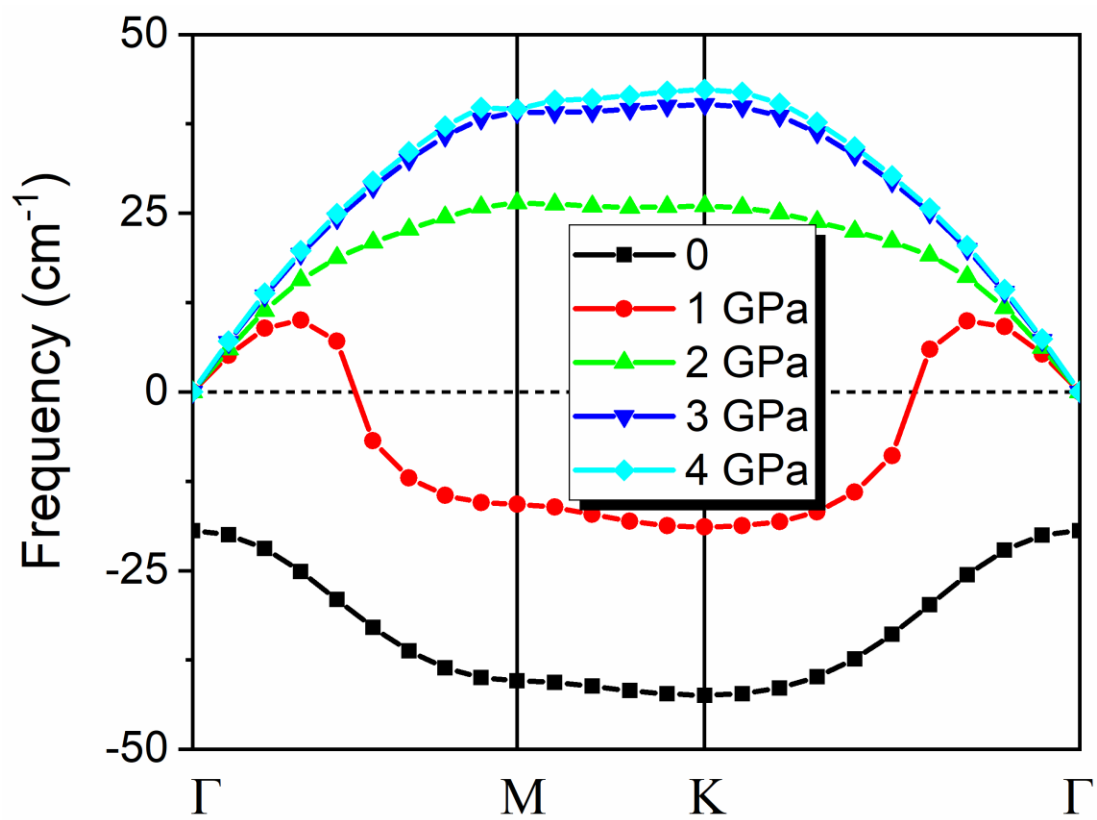
Fig. S9 Effect of external stress on the lowest phonon band.
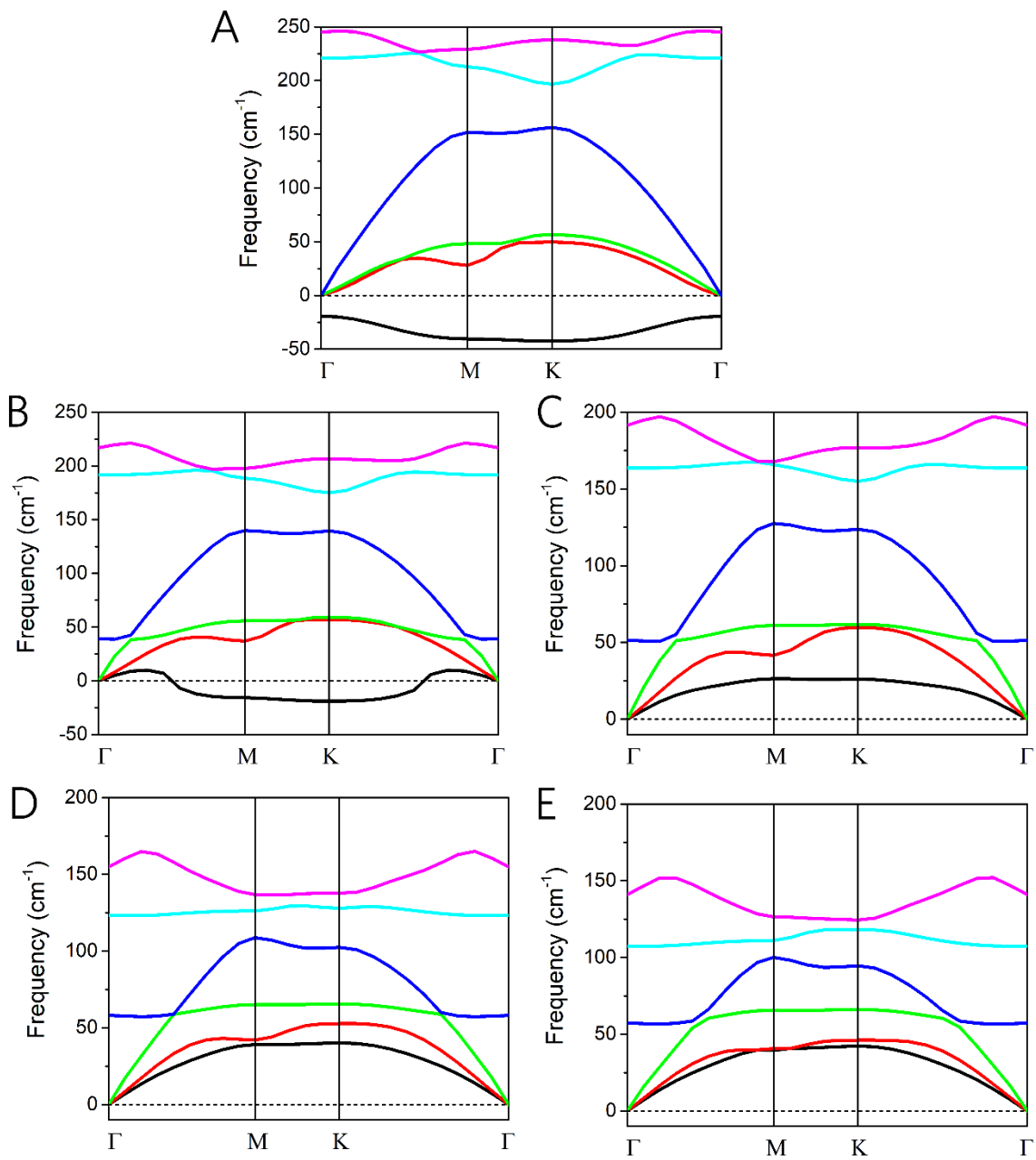
Fig. S10 Phonon dispersion of 2D CdSe monolayer under different external tensile stress.

(A) 0 GPa, (B) 1 GPa, (C) 2 GPa, (D) 3 GPa, (E) 4 GPa.
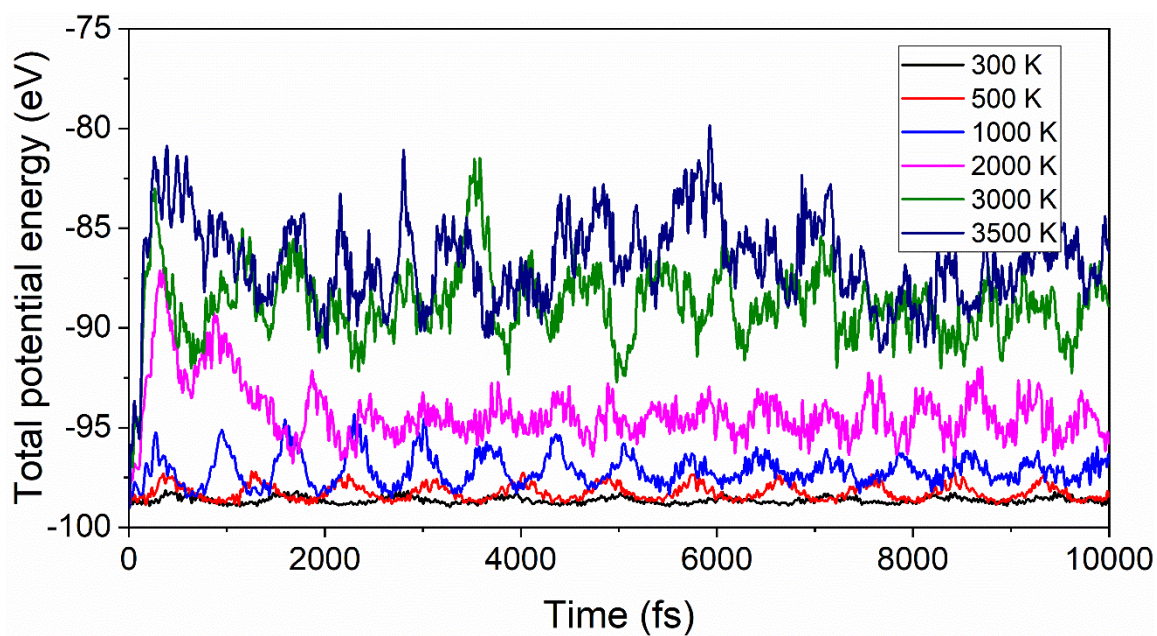
Fig. S11 Total potential energy of 2D SrO monolayer for 10 ps at different temperatures

during AIMD simulation.
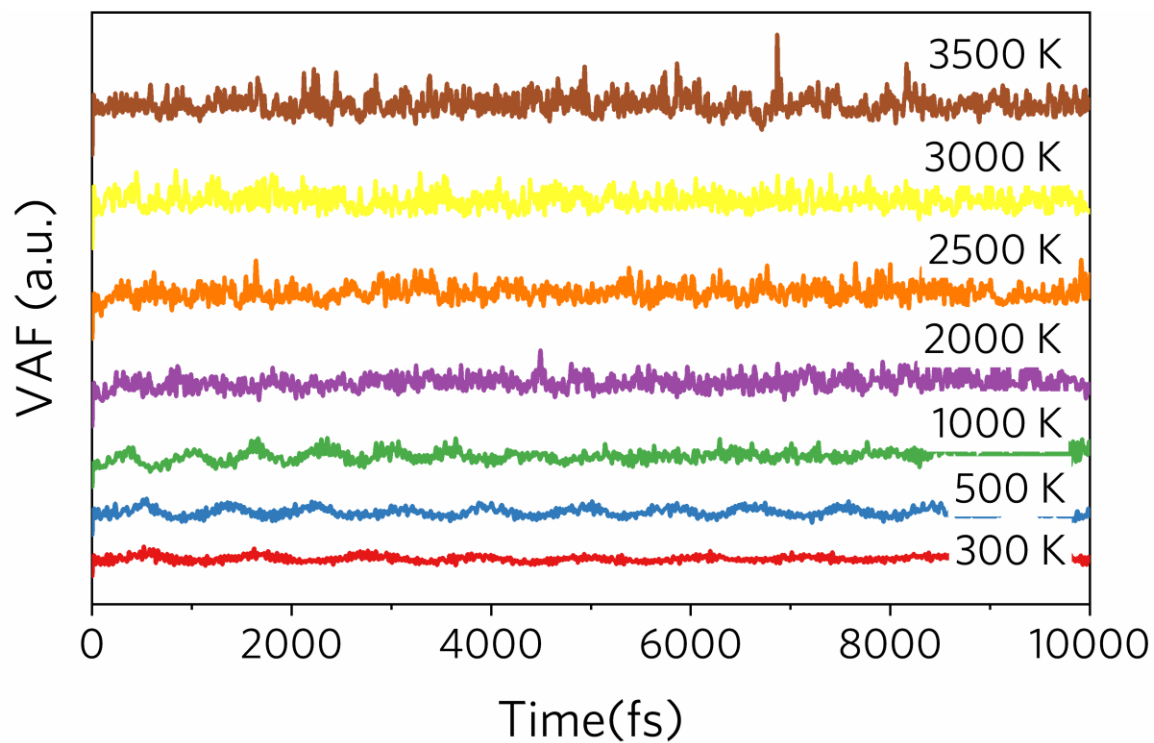
Fig. S12 Velocity autocorrelation function of 2D SrO monolayer for 10 ps at different

temperatures during AIMD simulation.
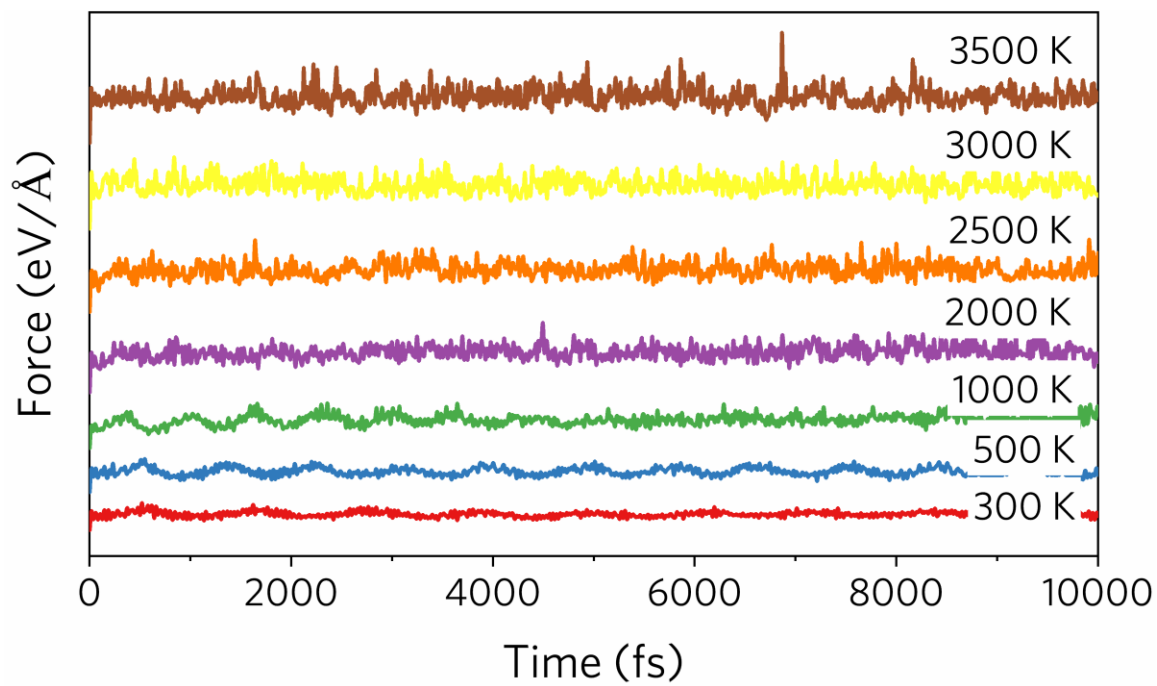
Fig. S13 Forces of 2D SrO monolayer for 10 ps at different temperatures during AIMD simulation.
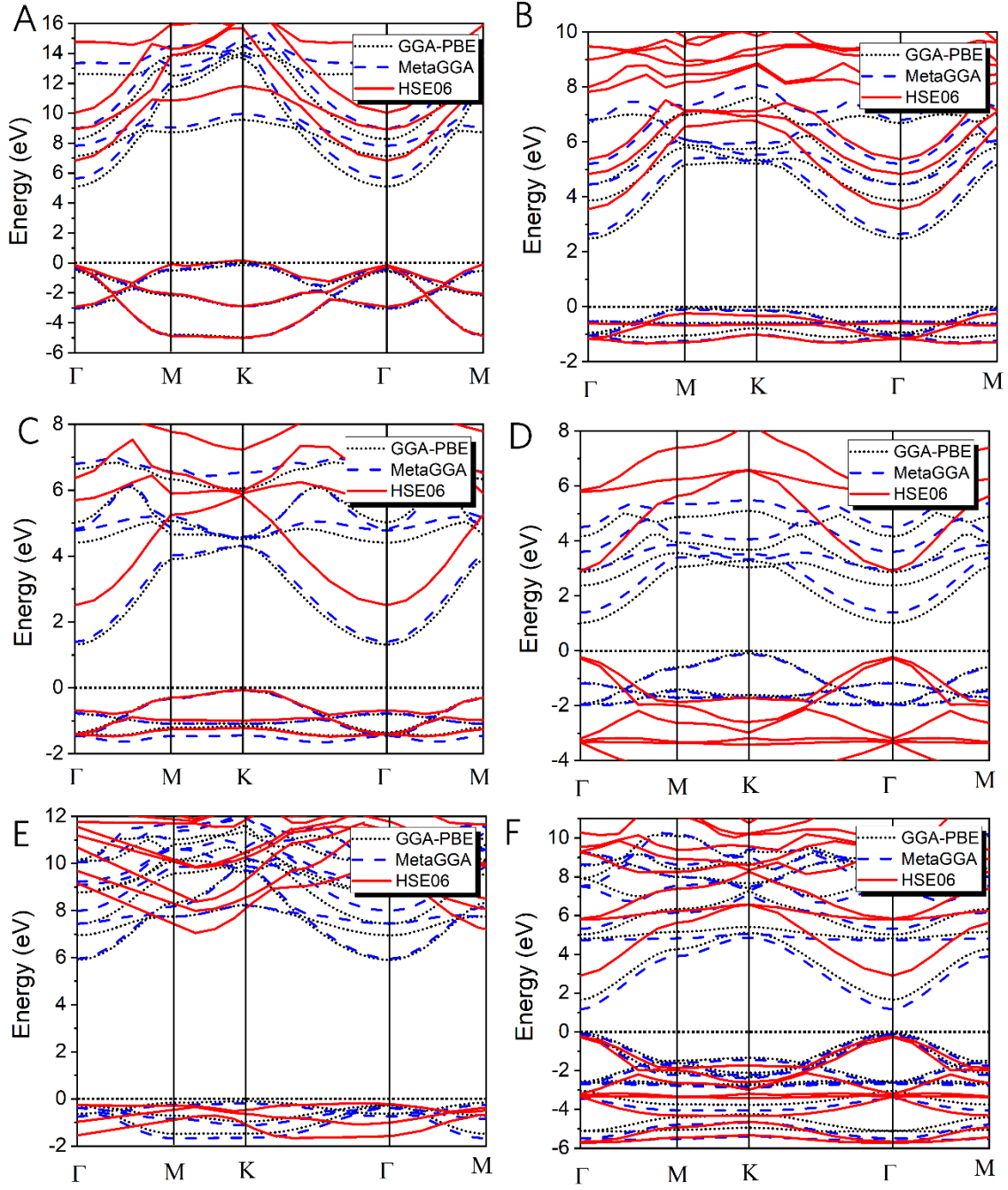
Fig. S14 Band structure of 2D monoxide and monochloride monolayers calculated using PAW-PBE, MetaGGA-SCAN, and HSE06 exchange functional. (A) BeO, (B) CaO, (C) SrO, (D) BaO, (E) LiCl, and (F) AgCl 2D monolayers.
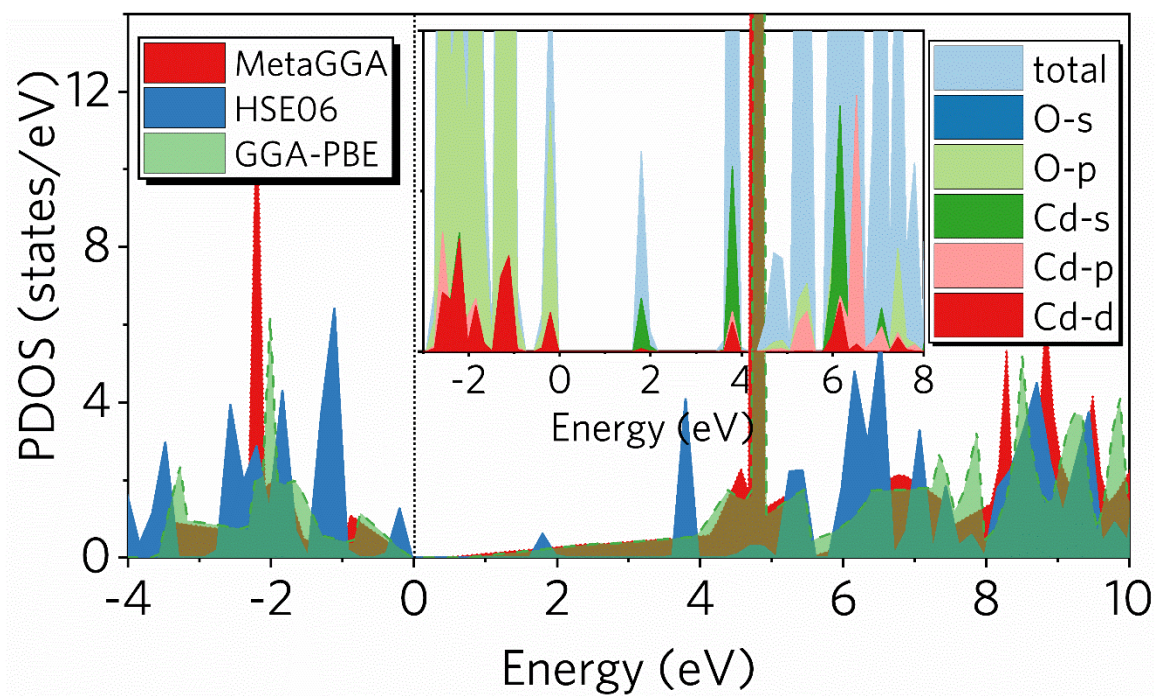
Fig. S15 Total density of states of 2D CdO monolayer using MetaGGA-SCAN, HSE06 and GGA-PBE, inset shows the partial density of states.
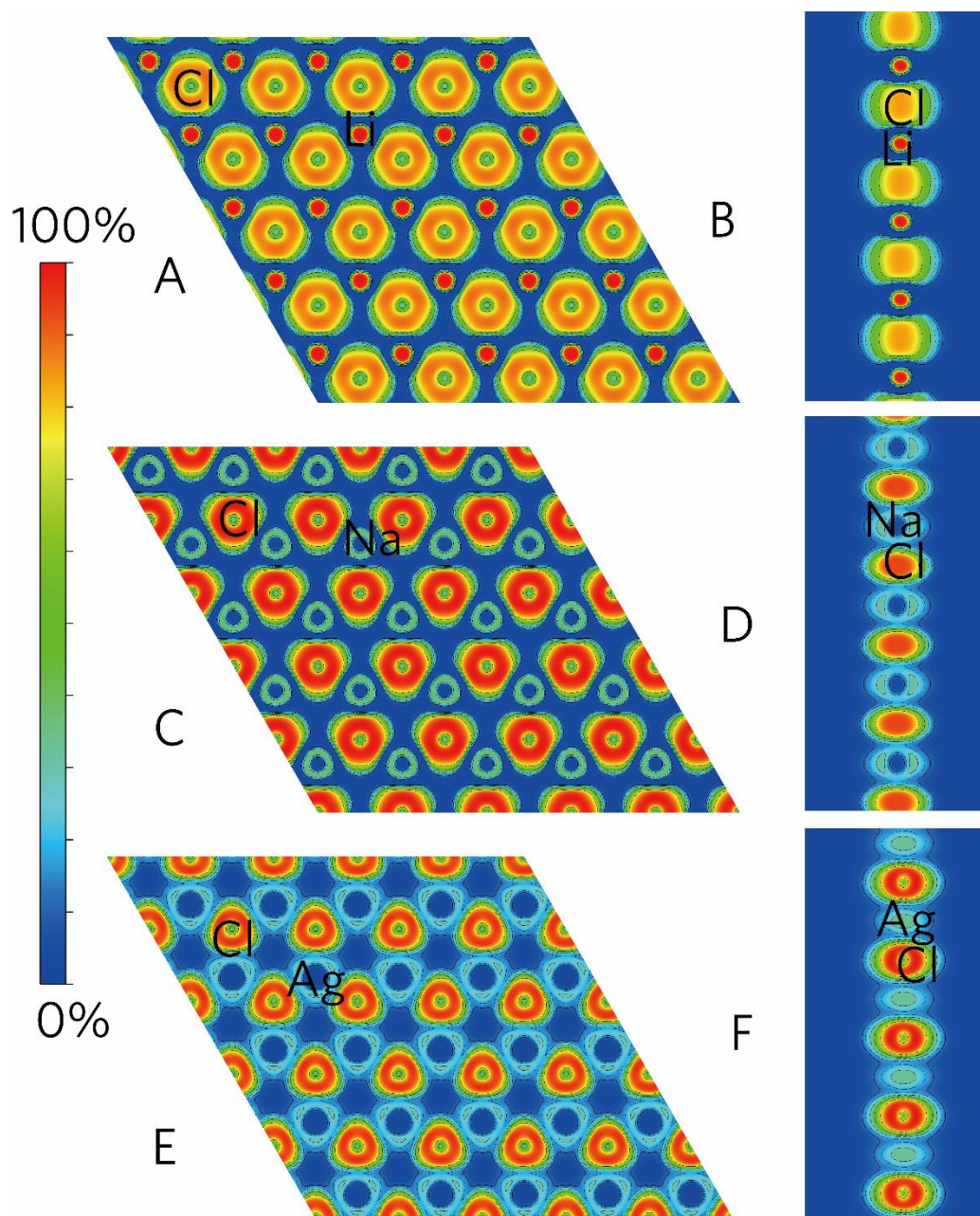
Fig. S16 Isosurfaces of electron localization function for (A, B) LiCl, (C, D) NaCl, and (E, F) AgCl in the top and side view.
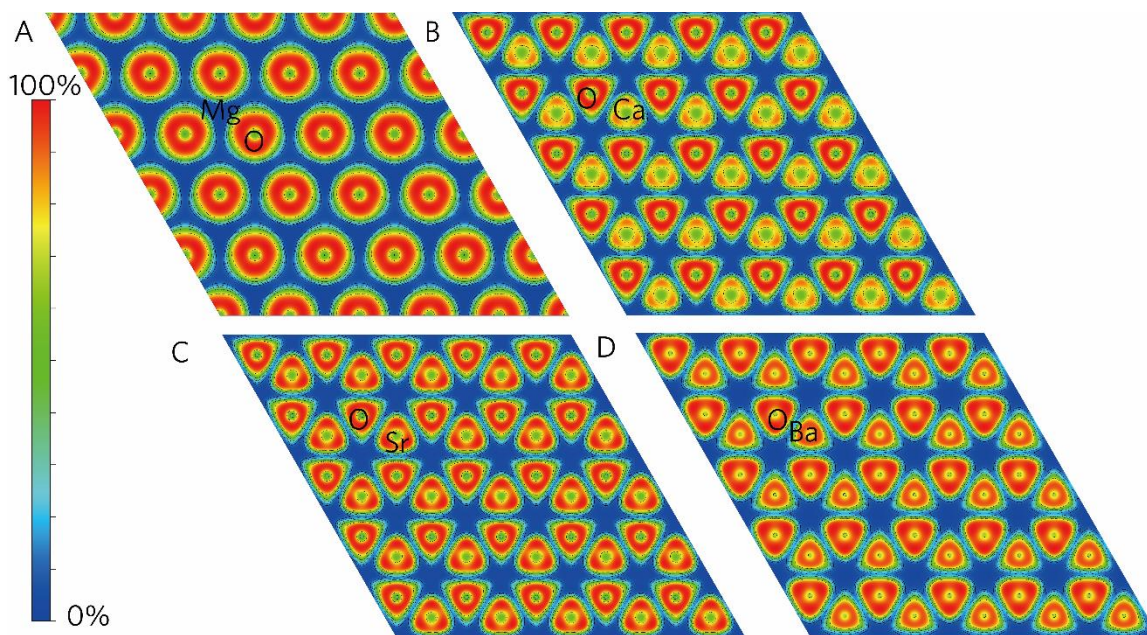
Fig. S17 Isosurfaces of electron localization function for 2D monoxide monolayers: (A)

MgO, (B) CaO, (C) SrO, and (D) BaO in the top view.
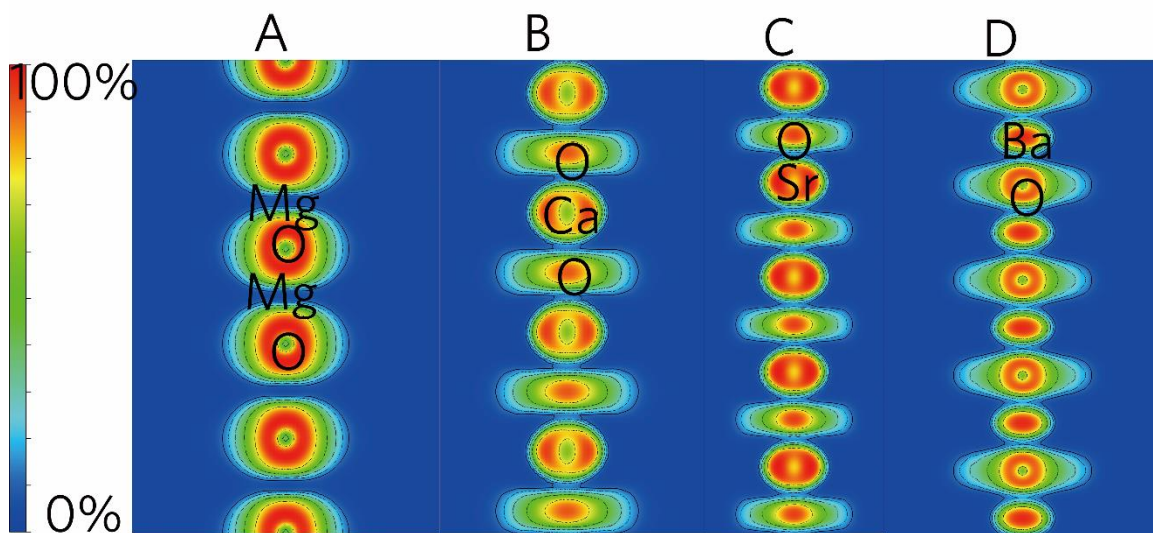
Fig. S18 Isosurfaces of electron localization function for 2D monoxide monolayers: (A) MgO, (B) CaO , (C) SrO, and (D) BaO in the side view.

Supplementary Tables

Table S1 Crystal lattice parameters of bulk rock-salt-like binary compounds.

Bulk materials	a, Å	b, Å	c, Å	α, °	β, °	γ, °	Reference
LiCl	5.1295	5.1295	5.1295	90	90	90	(44, 45)
NaCl	5.62	5.62	5.62	90	90	90	(46, 47)
AgCl	5.5463	5.5463	5.5463	90	90	90	(48)
BeO	3.796	3.796	3.796	90	90	90	(49)
MgO	4.217	4.217	4.217	90	90	90	(50)
CaO	4.799	4.799	4.799	90	90	90	(51)
SrO	5.1396	5.1396	5.1396	90	90	90	(51)
BaO	5.496	5.496	5.496	90	90	90	(49)
CdO	4.696	4.696	4.696	90	90	90	(52)
HfO	5.115	5.115	5.115	90	90	90	(45)

Table S2 Crystal lattice parameters of bulk rock-salt-like binary compounds.

2D materials	a, Å	b, Å	α, °	β, °	γ, °
LiCl	3.9185	3.9185	90	90	120
NaCl	4.5357	4.5357	90	90	120
AgCl	4.2316	4.2316	90	90	120
BeO	2.5958	2.5958	90	90	120
MgO	3.3057	3.3057	90	90	120
CaO	3.747	3.747	90	90	120
SrO	3.9884	3.9884	90	90	120
BaO	4.2552	4.2552	90	90	120
CdO	3.6476	3.6476	90	90	120

Table S3 Band gap (Eg) for 2D materials derived from HSE06 in comparison with experimental values for 3D materials in unit eV.

Materials	Eg 2D	Eg 3D
LiCl	7.221	9.4 [a]
NaCl	6.302	8.75 [b]
AgCl	3.129	3.25 [c]
BeO	6.846	10.6 [d]
MgO	4.76	7.8 [e]
CaO	3.801	7.09 [f]
SrO	2.74	5.9 [g]
BaO	2.153	5 [h]
CdO	2.08	2.46 [i]

a reference (53)

b reference (54)

c reference (55, 56)

d reference (57, 58)

e reference (59)

f reference (59, 60)

g reference (61)

h reference (62)

i reference (63)

Table S4 Cij matrix of 2D MgO monolayer, together with the corresponding eigenvalues.

System	*Cij*	*j=1*	*j=2*	*j=3*	*j=4*	*j=5*	*j=6*
	i=1	73.445	42.771	0.371	0	0	0
	i=2	42.771	73.445	0.371	0	0	0
MgO	*i=3*	0.371	0.371	0.934	0	0	0
	i=4	0	0	0	0.732	0	0
	i=5	0	0	0	0	0.732	0
	i=6	0	0	0	0	0	15.337
	Eigenvalues	116.219	30.674	0.932	0.732	0.732	15.337

Table S5 Cij matrix of 2D NaCl monolayer, together with the corresponding eigenvalues.

System	Cij	j=1	j=2	j=3	j=4	j=5	j=6
	i=1	10.444	8.179	0.397	0	0	0
	i=2	8.179	10.444	0.397	0	0	0
NaCl	i=3	0.397	0.397	0.309	0	0	0
	i=4	0	0	0	0.061	0	0
	i=5	0	0	0	0	0.061	0
	i=6	0	0	0	0	0	1.133
	Eigenvalues	18.641	2.265	0.292	0.061	0.061	1.133

Table S6 Bader charge, Mulliken charge, and Hirshfeld charge of the predicted 2D monolayer in unit e.

2D materials	Nominal charge	Bader charge	Mulliken charge	Hirschfeld Charge
LiCl	1	0.87555	0.94	0.23
NaCl	1	0.85254	0.69	0.34
AgCl	1	0.465	0.33	0.19
BeO	2	1.68292	0.94	0.31
MgO	2	1.618	1.21	0.5
CaO	2	1.452	1.1	0.53
SrO	2	1.52671	1.01	0.57
BaO	2	1.471	0.98	0.57
CdO	2	1.20193	0.98	0.45

References

1. Wang Y, Lv J, Zhu L, Ma Y (2012) CALYPSO: A method for crystal structure prediction. *Comput Phys Commun* 183(10):2063–2070.
2. Wang Y, Lv J, Zhu L, Ma Y (2010) Crystal structure prediction via particle-swarm optimization. *Phys Rev B* 82(9):094116.
3. Luo X, et al. (2011) Predicting two-dimensional boron-carbon compounds by the global optimization method. *J Am Chem Soc* 133(40):16285–16290.
4. Zhang H, Li Y, Hou J, Tu K, Chen Z (2016) FeB_6 monolayers: The graphene-like material with hypercoordinate transition metal. *J Am Chem Soc* 138(17):5644–5651.
5. Yang LM, et al. (2015) Two-dimensional Cu_2Si monolayer with planar hexacoordinate copper and silicon bonding. *J Am Chem Soc* 137(7):2757–2762.
6. Jiao Y, Ma F, Bell J, Bilic A, Du A (2016) Two-Dimensional Boron Hydride Sheets: High Stability, Massless Dirac Fermions, and Excellent Mechanical Properties. *Angew Chemie - Int Ed* 55(35):10292–10295.
7. Ma F, et al. (2016) Graphene-like Two-Dimensional Ionic Boron with Double Dirac Cones at Ambient Condition. *Nano Lett* 16(5):3022–3028.
8. Ming W, Yoon M, Du MH, Lee K, Kim SW (2016) First-Principles Prediction of Thermodynamically Stable Two-Dimensional Electrides. *J Am Chem Soc* 138(47):15336–15344.
9. Payne MC, Teter MP, Allan DC, Arias TA, Joannopoulos JD (1992) Iterative minimization techniques for ab initio total-energy calculations: Molecular dynamics and conjugate gradients. *Rev Mod Phys* 64(4):1045–1097.
10. Kleinman L, Bylander DM (1982) Efficacious form for model pseudopotentials. *Phys Rev Lett* 48(20):1425–1428.
11. Perdew JP, et al. (2008) Restoring the Density-Gradient Expansion for Exchange in Solids and Surfaces. *Phys Rev Lett* 100(13):136406.
12. Pfrommer BG, Côté M, Louie SG, Cohen ML (1997) Relaxation of Crystals with the Quasi-Newton Method. *J Comput Phys* 131(1):233–240.
13. Kresse G, Joubert D (1999) From ultrasoft pseudopotentials to the projector augmented-wave method. *Phys Rev B* 59(3):1758–1775.
14. Kresse G, Furthmüller J (1996) Efficient iterative schemes for *ab* initio total-energy calculations using a plane-wave basis set. *Phys Rev B* 54(16):11169–11186.
15. Monkhorst HJ, Pack JD (1976) Special points for Brillouin-zone integrations. *Phys Rev B* 13(12):5188–5192.
16. Krukau A V., Vydrov OA, Izmaylov AF, Scuseria GE (2006) Influence of the exchange screening parameter on the performance of screened hybrid functionals. *J Chem Phys* 125(22):1–5.
17. Heyd J, Scuseria GE, Ernzerhof M (2003) Hybrid functionals based on a screened Coulomb potential. *J Chem Phys* 118(18):8207–8215.
18. Refson K, Tulip PR, Clark SJ (2006) Variational density-functional perturbation theory for dielectrics and lattice dynamics. *Phys Rev B* 73(15):155114.
19. Hoover WG (1985) Canonical dynamics: Equilibrium phase-space distributions. *Phys Rev A* 31(3):1695–1697.

20. Nosé S (1984) A unified formulation of the constant temperature molecular dynamics methods. *J Chem Phys* 81(1):511–519.
21. Sanville E, Kenny SD, Smith R, Henkelman G (2007) Improved grid-based algorithm for Bader charge allocation. *J Comput Chem* 28(5):899–908.
22. Henkelman G, Arnaldsson A, Jónsson H (2006) A fast and robust algorithm for Bader decomposition of charge density. *Comput Mater Sci* 36(3):354–360.
23. Yu M, Trinkle DR (2011) Accurate and efficient algorithm for Bader charge integration. *J Chem Phys* 134(6):064111.
24. Segall MD, Shah R, Pickard CJ, Payne MC (1996) Population analysis of plane-wave electronic structure calculations of bulk materials. *Phys Rev B* 54(23):16317–16320.
25. Payne MDS and PJDL and MJP and CJP and PJH and SJC and MC (2002) First-principles simulation: ideas, illustrations and the CASTEP code. *J Phys Condens Matter* 14(11):2717.
26. Wiberg KB, Rablen PR (1993) Comparison of atomic charges derived via different procedures. *J Comput Chem* 14(12):1504–1518.
27. Hirshfeld FL (1977) Bonded-atom fragments for describing molecular charge densities. *Theor Chim Acta* 44(2):129–138.
28. Gonze X (1995) Adiabatic density-functional perturbation theory. *Phys Rev A* 52(2):1096–1114.
29. Tersoff J, Hamann DR (1983) Theory and application for the scanning tunneling microscope. *Phys Rev Lett* 50(25):1998–2001.
30. Wang G, Loh GC, Pandey R, Karna SP (2015) Novel Two-Dimensional Silica Monolayers with Tetrahedral and Octahedral Configurations. *J Phys Chem C* 119(27):15654–15660.
31. Zhang Y, et al. (2008) Giant phonon-induced conductance in scanning tunneling spectroscopy of gate-tunable graphene : Article : Nature Physics. *Nat Phys* 4:627.
32. Stolyarova E, et al. (2007) High-resolution scanning tunneling microscopy imaging of mesoscopic graphene sheets on an insulating surface. *Proc Natl Acad Sci* 104(22):9209 LP – 9212.
33. Mohr M, et al. (2007) Phonon dispersion of graphite by inelastic x-ray scattering. *Phys Rev B* 76(3):35439.
34. Maultzsch J, Reich S, Thomsen C, Requardt H, Ordejón P (2004) Phonon Dispersion in Graphite. *Phys Rev Lett* 92(7):75501.
35. Lazzeri M, Attaccalite C, Wirtz L, Mauri F (2008) Impact of the electron-electron correlation on phonon dispersion: Failure of LDA and GGA DFT functionals in graphene and graphite. *Phys Rev B* 78(8):81406.
36. Al Taleb A, Farías D (2016) Phonon dynamics of graphene on metals. *J Phys Condens Matter* 28(10):103005.
37. Castro Neto AH, Guinea F, Peres NMR, Novoselov KS, Geim AK (2009) The electronic properties of graphene. *Rev Mod Phys* 81(1):109–162.
38. Balandin DLN and AA (2012) Two-dimensional phonon transport in graphene. *J Phys Condens Matter* 24(23):233203.
39. Sun J, Ruzsinszky A, Perdew J (2015) Strongly Constrained and Appropriately Normed Semilocal Density Functional. *Phys Rev Lett* 115(3):36402.

40. Sun J, et al. (2013) Density Functionals that Recognize Covalent, Metallic, and Weak Bonds. *Phys Rev Lett* 111(10):106401.

41. Charles N, Rondinelli JM (2016) Assessing exchange-correlation functional performance for structure and property predictions of oxyfluoride compounds from first principles. *Phys Rev B* 94(17):174108.

42. Sun J, et al. (2016) Accurate first-principles structures and energies of diversely bonded systems from an efficient density functional. *Nat Chem* 8(9):831–836.

43. Meng Y, et al. (2016) When Density Functional Approximations Meet Iron Oxides. *J Chem Theory Comput* 12(10):5132–5144.

44. Präzisionsbestimmung von Gitterkonstanten hygroskopischer Verbindungen (LiCl, NaBr) (1938) *Zeitschrift für Phys Chemie* 40B:146.

45. Wyckoff RWG (1963) Interscience Publishers, New York, New York rocksalt structure. *Cryst Struct* 1:85–237.

46. Abrahams SC, Bernstein JL (1965) Accuracy of an automatic diffractometer. Measurement of the sodium chloride structure factors. *Acta Crystallogr* 18(5):926–932.

47. Juhás P, Farrow CL, Yang X, Knox KR, Billinge SJL (2015) Complex modeling: a strategy and software program for combining multiple information sources to solve ill posed structure and nanostructure inverse problems. *Acta Crystallogr Sect A* 71(6):562–568.

48. Hull S, Keen DA (1999) Pressure-induced phase transitions in AgCl, AgBr, and AgI. *Phys Rev B* 59(2):750–761.

49. Gerlach W (1922) Die Gitterstruktur der Erdalkalioxyde. *Zeitschrift für Phys* 9(1):184–192.

50. SASAKI S, FUJINO K, TAKÉUCHI Y (1979) X-ray determination of electron-density distributions in oxides, MgO, MnO, CoO, and NiO, and atomic scattering factors of their constituent atoms. *Proc Japan Acad Ser B* 55(2):43–48.

51. Primak W, Kaufman H, Ward R (1948) X-Ray Diffraction Studies of Systems Involved in the Preparation of Alkaline Earth Sulfide and Selenide Phosphors1. *J Am Chem Soc* 70(6):2043–2046.

52. Zhang J (1999) Room-temperature compressibilities of MnO and CdO: further examination of the role of cation type in bulk modulus systematics. *Phys Chem Miner* 26(8):644–648.

53. Kunz AB (1982) Study of the electronic structure of twelve alkali halide crystals. *Phys Rev B* 26(4):2056–2069.

54. Brown FC, et al. (1970) Extreme-Ultraviolet Spectra of Ionic Crystals. *Phys Rev B* 2(6):2126–2138.

55. Xiong Z, et al. (2017) Electrochemical half-reaction-assisted sub-bandgap photon sensing in a graphene hybrid phsotodetector. *Npg Asia Mater* 9:e436.

56. Daupor H, Chenea A (2017) Degradation of blue and red inks by Ag/AgCl photocatalyst under UV light irradiation. *AIP Conf Proc* 1868(1):20009.

57. Sashin VA, Bolorizadeh MA, Kheifets AS, Ford MJ (2003) Electronic band structure of beryllium oxide. *J Phys Condens Matter* 15(21):3567–3581.

58. Emeline AV, Kataeva GV, Ryabchuk VK, Serpone N (1999) Photostimulated Generation of Defects and Surface Reactions on a Series of Wide Band Gap Metal-Oxide Solids. *J Phys Chem B* 103(43):9190–9199.

59.   Heo S, et al. (2015) Band gap and defect states of MgO thin films investigated using reflection electron energy loss spectroscopy. *AIP Adv* 5(7):77167.

60.   Kotani T (1994) Exact exchange-potential band-structure calculations by the LMTO-ASA method: MgO and CaO. *Phys Rev B* 50(20):14816–14821.

61.   Rao AS, Kearney RJ (1979) Logarithmic derivative reflectance spectra of BaO and SrO. *Phys status solidi* 95(1):243–250.

62.   McKee RA, Walker FJ, Chisholm MF (2001) Physical structure and inversion charge at a semiconductor interface with a crystalline oxide. *Science* 293(5529):468–471.

63.   Subramanyam TK, Uthanna S, Srinivasulu Naidu B (1998) Preparation and characterization of CdO films deposited by dc magnetron reactive sputtering. *Mater Lett* 35(3):214–220.